

Off-diagonal matrix elements of local operators in many-body quantum systems

Wouter Beugeling, Roderich Moessner, and Masudul Haque

Max-Planck-Institut für Physik komplexer Systeme, Nöthnitzer Straße 38, 01187 Dresden, Germany

(Dated: April 30, 2022)

In the time evolution of isolated quantum systems out of equilibrium, local observables generally relax to a long-time asymptotic value, governed by the expectation values (diagonal matrix elements) of the corresponding operator in the eigenstates of the system. The temporal fluctuations around this value, response to further perturbations, and the relaxation toward this asymptotic value, are all determined by the off-diagonal matrix elements. Motivated by this non-equilibrium role, we present generic statistical properties of off-diagonal matrix elements of local observables in two families of interacting many-body systems with local interactions. Since integrability (or lack thereof) is an important ingredient in the relaxation process, we analyze models that can be continuously tuned to integrability.

I. INTRODUCTION

The topic of non-equilibrium dynamics of thermally isolated quantum systems has enjoyed a resurgence of interest, partly because of experimental progress with cold atoms. An isolated system has no relaxation mechanism toward the low-lying parts of the many-body spectrum. As a result, the properties of eigenstates far from the edges of the spectrum may be more important for a non-equilibrium experiment than the low-energy parts of the spectrum, which is the traditional focus of interest of many-body quantum theory.

A key question in the non-equilibrium dynamics of isolated quantum systems is the thermalization or relaxation of a system prepared far out of equilibrium and subject to a time-independent Hamiltonian [1–66]. The value (if any) to which local observables relax is determined by the diagonal matrix elements $A_{\alpha\alpha} = \langle \psi_\alpha | \hat{A} | \psi_\alpha \rangle$ of the corresponding operator \hat{A} in the eigenstates $|\psi_\alpha\rangle$. The eigenstate thermalization hypothesis (ETH) states that the mechanism by which non-integrable (“chaotic”) systems thermalize is the smoothness of $A_{\alpha\alpha}$ as a function of eigenenergies E_α [1–3]. Accordingly, diagonal matrix elements of local operators have been the subject of several studies [3–7].

Off-diagonal matrix elements, $A_{\alpha\beta} = \langle \psi_\alpha | \hat{A} | \psi_\beta \rangle$, provide further information about the time evolution $\langle A \rangle(t)$ of observables. In any finite system initially prepared in a combination of many eigenstates, there will be residual temporal fluctuations around the long-time average. These temporal fluctuations have been the subject of several recent studies, both numerical [3, 9–14] and analytical [15, 16, 18]. The magnitude of these fluctuations is determined by $|A_{\alpha\beta}|^2$, weighted, of course, by the weights of the eigenstates in the non-equilibrium initial state. Autocorrelation functions (unequal-time correlators), interesting on their own and appearing in the formulation of fluctuation-dissipation relations in the “relaxed” state a long time after a quench [19], also are given in terms of $|A_{\alpha\beta}|^2$. Finally, the details of the temporal approach to the final relaxed value are also determined by the off-diagonal matrix elements of the corresponding operator [9]. The approach toward the final value has been calculated in some model systems [20, 21], although the connection to off-diagonal matrix elements has not been explored in detail.

The (statistical) properties of off-diagonal matrix elements of local operators, $A_{\alpha\beta}$, are thus related to a range of temporal properties of contemporary interest. In this work, we provide a statistical study of these objects. We use Hamiltonians that can be tuned between integrable limits, and provide scaling analyses as a function of system size. We thus study what happens to the distributions of $A_{\alpha\beta}$ as a function of distance from integrability, as well as how the thermodynamic limit is approached.

Some statistical aspects of off-diagonal matrix elements $A_{\alpha\beta}$ have appeared in Ref. [19] in the context of a non-equilibrium fluctuation-dissipation relation, and in Ref. [6]. The aim of the present paper is to focus directly on the $A_{\alpha\beta}$ in a manner independent of quench protocol and provide a thorough study of their statistical properties.

In the time evolution $\langle A \rangle(t)$, each matrix element $A_{\alpha\beta}$ contributes with a frequency equal to the eigenvalue difference $E_\beta - E_\alpha$ [19, 22, 23]. In many quenches of physical interest, the initial occupancies are confined to a small energy window (e.g., [3, 24, 25]). We therefore pay particular attention to the behavior of $A_{\alpha\beta}$ for small $E_\beta - E_\alpha$. At large frequencies, the average $|A_{\alpha\beta}|$ falls off fast, exponentially or super-exponentially with $E_\beta - E_\alpha$.

We identify signatures of the $A_{\alpha\beta}$ typical to the integrable, close-to-integrable, and nonintegrable cases. Close to integrability, we show that the matrix $|A_{\alpha\beta}|$ has a block-like or banded structure as a function of the energy difference (frequency) $E_\beta - E_\alpha$, which is visible as oscillatory behavior in the frequency-dependence of average $|A_{\alpha\beta}|^2$ values.

We show that the distribution of the matrix elements in any small frequency window is peaked around zero, having a near-gaussian form for generic non-integrable systems (cf. Ref. [6]). At or near integrability, there is a stronger peak around zero, i.e., the probability distribution is a mixture of two gaussian-like curves with unequal widths. This difference appears to be a basic distinction between generic (non-integrable) and integrable systems. We demonstrate how the proximity to integrability can be quantitatively characterized through the shape of the distribution of $A_{\alpha\beta}$ values, e.g., through the size dependence of the kurtosis of this distribution.

We find that the scaling behavior of the average value of $|A_{\alpha\beta}|^2$ is D^{-1} in terms of the Hilbert-space dimension D . The values of $|A_{\alpha\beta}|^2$ at low frequencies tend to be larger

than for the generic matrix elements, but the scaling follows D^{-1} as well. The scaling analysis is analogous to studies of the diagonal matrix elements or eigenstate expectation values, $A_{\alpha\alpha}$, as a function of system size, performed, e.g., in Refs. [6, 7]. As for the diagonal fluctuations [7, 42], we can construct plausibility arguments based on an assumption of quasi-randomness of the vector coefficients of the energy eigenstates. As such assumptions are difficult to prove rigorously, we emphasize, as in Ref. [7], that such arguments are inherently heuristic and that extensive, multi-system, numerical analysis is required to establish scaling laws; this paper provides such data.

The size dependence of $A_{\alpha\beta}$'s is related to the size dependence of the magnitude of the temporal fluctuations around the long-time average [11, 12, 14]. The D^{-1} scaling is consistent with the exponential dependence of the long-time fluctuations on the system size [14].

This paper is structured as follows. In Sec. II, we introduce our models: the XXZ ladder and the Bose-Hubbard chain. In Sec. III, we introduce the frequency-resolved average of the off-diagonal matrix elements. In Sec. IV, we analyze the distribution of values of $A_{\alpha\beta}$, characterizing how a mixed distribution (with two components having different widths) emerges close to integrability. Sec. V provides a scaling analysis of the size-dependence of the average values of $|A_{\alpha\beta}|^2$, focusing on the low-frequency matrix elements. Sections III, IV, and V show results for the XXZ ladder. We support the generality of these results by presenting corresponding data for the Bose-Hubbard chain in Sec. VI. In the appendices, we provide details of the relationship between time evolution $\langle A \rangle(t)$ and the matrix elements $A_{\alpha\beta}$, and about our quantification of the non-gaussian distributions.

II. MODELS AND OBSERVABLES

We use two families of Hamiltonians, each of which can be tuned to integrable points. Both have been used in our previous work on diagonal matrix elements [7]. Because we are interested in generic properties of matrix elements, we take care to avoid spurious symmetries in our model systems.

The first model is the spin- $\frac{1}{2}$ Heisenberg XXZ ladder with the geometry introduced in Ref. [7]. One ladder leg has an extra site compared to the other. There are thus $L = 2p + 1$ sites, with p rungs between the legs. This geometry avoids reflection symmetries. We have nearest-neighbor Heisenberg couplings

$$h_{i,j} = \frac{1}{2} (S_i^+ S_j^- + S_i^- S_j^+) + \Delta S_i^z S_j^z, \quad (1)$$

with $S_i^\pm = S_i^x \pm iS_i^y$, where S_i^μ ($\mu = x, y, z$) are the spin operators, and i, j denote the nearest-neighbor site pairs. The anisotropy parameter Δ is kept away from special values like 0 and ± 1 , in order to avoid $SU(2)$ symmetry or special solvable points; we use $\Delta = 0.8$. The Hamiltonian of the system

is $H = H_0 + \lambda H_1$, where

$$H_0 = \sum_{i=1}^{p-1} h_{i,i+1} + \sum_{i=p}^{2p} h_{i,i+1} \quad \text{and} \quad H_1 = \sum_{i=1}^p h_{i,i+p} \quad (2)$$

are the intrachain (leg) and the interchain (rung) coupling, respectively. The rung coupling is multiplied by λ , which acts as a tuning parameter. The xy coupling along the ladder legs sets the units of energy and frequency. For $\lambda = 0$, the chains are uncoupled and the model is integrable. For finite values of λ , the system is non-integrable. In the limit of large λ , where the rung couplings dominate, there is another integrable limit. The effect of varying λ on the fluctuations of diagonal matrix elements has been studied in detail in Ref. [7].

The number N_\uparrow of up spins is a conserved quantity. The analysis can therefore be constrained to a fixed- N_\uparrow sector. The dimension of the Hilbert space of the (L, N_\uparrow) sector is equal to the binomial coefficient $D = \binom{L}{N_\uparrow}$. In order to study scaling, we use a sequence of system sizes with almost constant filling fraction. We present data for a sequence of systems with near-zero magnetization (near half filling), by choosing $L = 2p + 1$ and $N_\uparrow = p$ for integer p .

Discussion of thermalization generally concerns local observables. We present data for S_2^z and $S_2^z S_{p+2}^z$, which serve as representative examples of single-site and two-site operators.

The second tunable Hamiltonian is the Bose-Hubbard model on an L -site chain, with an extra term at an edge site killing reflection symmetry, as in Ref. [7]. The Hamiltonian is

$$H_{\text{BH}} = \sum_{i=1}^{L-1} (b_i^\dagger b_{i+1} + b_{i+1}^\dagger b_i) + \lambda \left(\sum_i b_i^\dagger b_i^\dagger b_i b_i + H_\Delta \right) \quad (3)$$

where b_i is the creation operator at site i and $H_\Delta = \Delta b_1^\dagger b_1^\dagger b_1 b_1$ with $\Delta = 0.1$ is a small perturbation to the interaction term at the first site. The system is integrable in the $\lambda \rightarrow 0$ and $\lambda \rightarrow \infty$ limits, and nonintegrable for intermediate values. We show results for the sector of unit filling fraction, i.e., the number of bosons $N_b = L$. This choice provides the same sequence of Hilbert-space sizes [for bosons, $D = \binom{L+N_b-1}{N_b}$] as the one given by $L = 2N_\uparrow + 1$ for the XXZ ladder. Typical local observables in the study of this model include $n_i = b_i^\dagger b_i$, $b_i^\dagger b_{i+1} + b_{i+1}^\dagger b_i$ and $n_i n_{i+1}$.

III. FREQUENCY-RESOLVED AVERAGE MATRIX ELEMENTS

In Fig. 1, we visualize through a density plot the structure of the matrix $|A_{\alpha\beta}|$ as a function of energies E_α and E_β , using the rung correlator $\hat{A} = S_2^z S_{p+2}^z$ of the XXZ ladder as observable. The diagonal matrix elements are not considered. The structure of darker bands parallel to the main diagonal suggests that the magnitude of the $|A_{\alpha\beta}|$ depends roughly on the difference $E_\alpha - E_\beta$. Thus the energies (E_α, E_β) rather than the indices (α, β) are natural coordinates for this plot (cf. Ref. [9]).

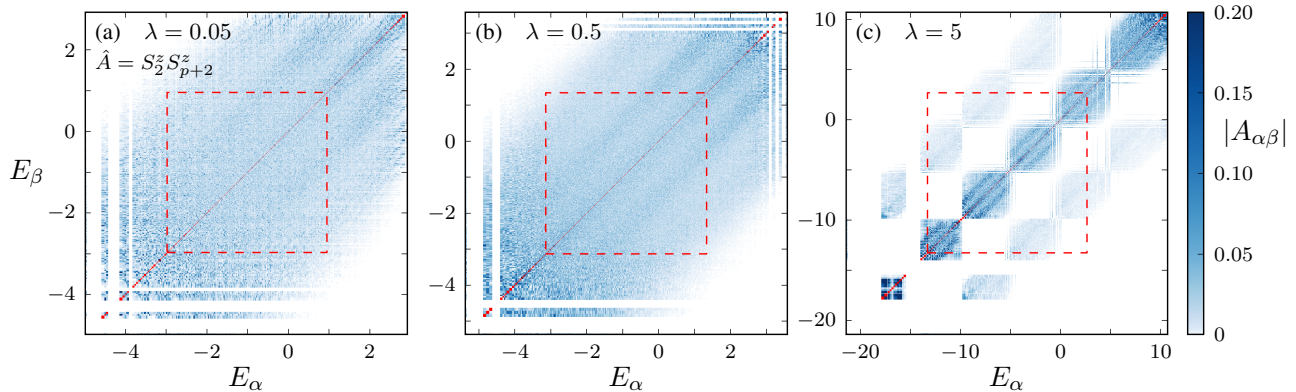


FIG. 1. Matrix structure of $|A_{\alpha\beta}|$ as function of E_{α} and E_{β} for the observable $\hat{A} = S_2^z S_{p+2}^z$. The diagonal matrix elements are ignored. The white bands near the edges are regions without eigenvalues. The red dashed square indicates the central half of the energy range, i.e., $[\frac{3}{4}E_{\min} + \frac{1}{4}E_{\max}, \frac{1}{4}E_{\min} + \frac{3}{4}E_{\max}]$ in each direction: this is the “bulk” of the spectrum on which we focus our analysis. The system size is $(L, N_{\uparrow}) = (13, 6)$; the Hilbert space dimension is $D = 1716$. The unit of energy is set by the xy coupling along the ladder legs.

To consider the $|A_{\alpha\beta}|$ from finite-size data as a continuous function of frequency, we “smooth out” $|A_{\alpha\beta}|^2 \delta(\omega - (E_{\beta} - E_{\alpha}))$ as a function of ω , by averaging the values of $|A_{\alpha\beta}|^2$ with $E_{\alpha} - E_{\beta}$ in the frequency window $[\omega - \Delta\omega, \omega + \Delta\omega]$,

$$S_A^2(\omega, \Delta\omega) \equiv \frac{1}{\tilde{N}_{\omega, \Delta\omega}} \sum_{\substack{\alpha, \beta \\ \alpha \neq \beta \\ E_{\alpha} - E_{\beta} \in [\omega - \Delta\omega, \omega + \Delta\omega]}} |A_{\alpha\beta}|^2, \quad (4)$$

where $\tilde{N}_{\omega, \Delta\omega}$ is the number of state pairs satisfying $E_{\alpha} - E_{\beta} \in [\omega - \Delta\omega, \omega + \Delta\omega]$. The frequency-window width $2\Delta\omega$ is chosen such that the interval contains sufficiently many pairs of states. We restrict ourselves to positive ω , since $A_{\alpha\beta} = A_{\beta\alpha}$ for hermitian observables. The quantity $S_A^2(\omega)$ is closely related to fluctuations around the asymptotic value to which $\langle A(t) \rangle$ relaxes a long time after a quantum quench (Appendix A). The quantity $S_A(\omega, \Delta\omega)$ is the standard deviation of the distribution formed by the $A_{\alpha\beta}$ in the frequency window.

In the large-system limit, the number of states in the window is approximately proportional to the *density of pairs*

$$\tilde{\rho}(\omega) = \int \rho(E)\rho(E - \omega)dE \quad (5)$$

through $\tilde{N}_{\omega, \Delta\omega} \approx 2\Delta\omega\tilde{\rho}(E)$. The density of pairs is the autocorrelation of the density of states $\rho(E)$ with itself. The behavior of $\tilde{\rho}(\omega)$ is shown in the bottom row of Figure 2 for the spin ladder system, for different values of the λ parameter.

To distinguish frequency regimes, we define a “typical” frequency scale ω_0 , as the root-mean-square of all possible frequencies:

$$\omega_0^2 = \text{var}(E_{\alpha} - E_{\beta}) = \frac{1}{D^2} \sum_{\alpha, \beta} (E_{\alpha} - E_{\beta})^2 = 2 \text{var}(E_{\alpha}). \quad (6)$$

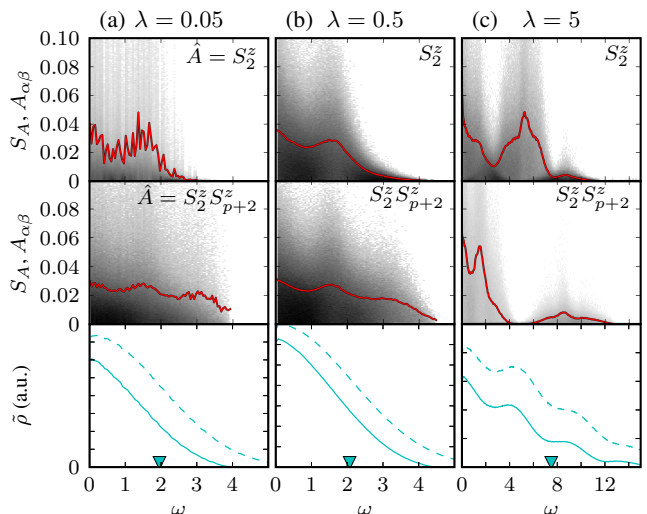


FIG. 2. Frequency-resolved analysis of off-diagonal elements for the $(L, N_{\uparrow}) = (13, 6)$ ladder. The shadings show the distribution of the values of $|A_{\alpha\beta}|$ for each frequency window; darker shading indicates more occurrences of respective $|A_{\alpha\beta}|$ values. The curves show S_A as a function of the frequency ω . In the bottom panel, we indicate the density of pairs $\tilde{\rho}$ for the central part of the spectrum (solid) and for the full spectrum (dashed), in arbitrary units. The marker on the horizontal axis points to the typical frequency ω_0 . The shading and solid curves are all results using the central part of the spectrum. The units of frequency are the same as the units used for energy in Fig. 1.

In Fig. 2, the values ω_0 are indicated by markers on the horizontal (frequency) axes.

The frequency dependence of $S_A(\omega)$ is shown in Fig. 2 for the observables $\hat{A} = S_2^z$ and $\hat{A} = S_2^z S_{p+2}^z$ in the XXZ ladder model. In addition, through the shading in the top two panels, we indicate the distribution of the values of $|A_{\alpha\beta}|$ in each frequency window. The value of $\Delta\omega = 0.05$ used in this figure

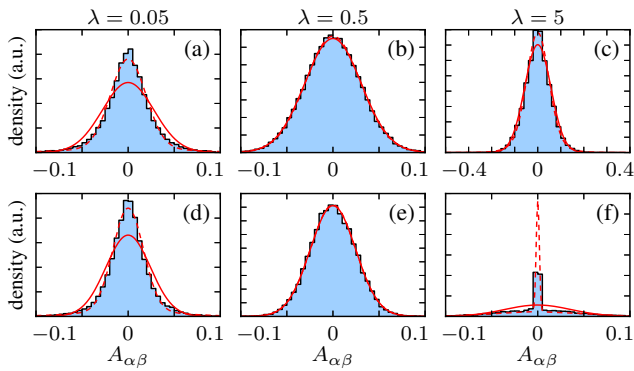


FIG. 3. Histograms of the off-diagonal elements $A_{\alpha\beta}$ with (a–c) $E_\beta - E_\alpha \in (0, 0.05\omega_0)$ and (d–f) $E_\beta - E_\alpha \in [0.25\omega_0, 0.25\omega_0 + \delta\omega)$, where $\delta\omega = 0.05$. The solid curve is a gaussian fit and the dashed curve is the fit to a mixture of two gaussians, Eq. (8). The observable is $\hat{A} = S_2^z S_{p+2}^z$ and the system size is $(L, N_\uparrow) = (13, 6)$. The number of state pairs in these histogram computations ranges from 4000 to 50000.

is a compromise between being sufficiently small to resolve the details, and having sufficiently many state pairs for good statistics. In the cases of Fig. 2, the number of state pairs in the window $[\omega - \Delta\omega, \omega + \Delta\omega]$ is $\sim 10^4$ for $\omega \lesssim \omega_0$.

At high frequencies ($\omega \gg \omega_0$), $S_A(\omega)$ decreases as a function of ω . The decrease is rapid; we have found this to be generally exponential or super-exponential (\sim gaussian) with ω ; the details vary with the observable and appear to be non-universal.

At medium frequencies, $S_A(\omega)$ typically shows several peaks. The oscillatory behavior is more pronounced near integrability, i.e., for small and large λ . We observe typical small- λ behaviour in Fig. 2(a): The quantity S_A shows short-scale oscillations, while the density of pairs $\tilde{\rho}(\omega)$ is smooth. We conjecture that the oscillatory behavior in near-integrable systems is due to the Hamiltonian being decomposable into many weakly coupled sectors. Whenever α and β are in different sectors, $A_{\alpha\beta} \approx 0$.

At large λ , the system splits into weakly coupled sectors which are in addition separated in energy, as evidenced by the block-like structure in Fig. 1(c). Thus, the peaks of S_A are accompanied by those in the density of pairs $\tilde{\rho}(\omega)$. The blocks are separated by energy $\sim \lambda$, which can be understood from treating the system as uncoupled dimers in the $\lambda \rightarrow \infty$ limit. These are also the approximate frequencies at which peaks can be seen in Fig. 2(c).

IV. DISTRIBUTION OF OFF-DIAGONAL MATRIX ELEMENTS

Having described the variance $S_A^2(\omega)$ of the distribution of the values of $A_{\alpha\beta}$, we now look at the full distribution.

In Fig. 2, we have shown using shading densities the frequency-resolved distributions of values of $|A_{\alpha\beta}|^2$. A feature visible already in the density plots is that the distributions are more strongly weighted near zero (near the horizon-

tal axis) near integrability. This feature will be explored and described in more detail below.

In Fig. 3, we show the distributions of $A_{\alpha\beta}$ values, in two different frequency windows. The top panels show the low-frequency regime (cutoff frequency $\omega_{\max} = 0.05\omega_0$). The bottom panels focus on a frequency window around $0.25\omega_0$. Only the states in the central part of the spectrum (within the dashed square region in Fig. 1) are considered.

The distributions are seen to be very nearly symmetric around zero. Of course, the signs of individual $A_{\alpha\beta}$ values are not meaningful since every eigenstate carries an arbitrary phase. However, from $N \gg 1$ eigenstates, one obtains $\frac{1}{2}N^2 \gg N$ matrix elements; so the overall shape of the distribution (roughly equal number of positive and negative values) cannot be altered by the choice of phases for the eigenstates.

The solid curves are gaussian fits determined by the variance of the $A_{\alpha\beta}$, centered at 0. Far from integrability, this is seen to be a very good description. However, near integrability the distribution has a sharper peak than a gaussian, and appears to be a mixture of two near-gaussian distributions with different widths. This appears to be a fundamental distinction between (near-)integrable and generic systems. The additional weight around zero can be understood as follows: the integrable spectrum is divided into symmetry sectors and eigenstates belonging to different sectors are at best weakly coupled through local operators, i.e., $A_{\alpha\beta}$ is close to zero whenever α and β belong to different sectors.

The gaussian shape of the distributions for generic non-integrable points can be explained heuristically by invoking the central limit theorem. Writing $c_\gamma^{(\alpha)} \equiv \langle \phi_\gamma | \psi_\alpha \rangle$ in terms of the eigenstates $|\psi_\alpha\rangle$ of the Hamiltonian and $|\phi_\gamma\rangle$ of A (with eigenvalues a_γ), we can write the matrix elements as

$$A_{\alpha\beta} = \sum_\gamma c_\gamma^{(\alpha)*} c_\gamma^{(\beta)} a_\gamma. \quad (7)$$

For non-integrable systems, the summand $c_\gamma^{(\alpha)*} c_\gamma^{(\beta)} a_\gamma$ may be expected to behave like a random variable. The central limit theorem then implies the gaussian distribution of $A_{\alpha\beta}$. As in Ref. [7], we stress that the randomness of coefficients is a hypothesis and difficult to prove rigorously. This is in the same spirit as arguments for scaling behaviors of diagonal matrix elements or of inverse participation ratios based on similar randomness assumptions [7, 42].

In order to characterize the nature of the distributions at small and large λ , we fit the numerically obtained histograms to the sum of two gaussian distributions, defined as

$$g(A) = an_{\sigma_1}(A) + (1-a)n_{\sigma_2}(A), \quad (8)$$

where $n_{\sigma_i}(A)$ is the gaussian distribution with variance σ_i^2 and zero mean, and $0 \leq a \leq 1$. There are three fit parameters, a , σ_1 , and σ_2 (with $\sigma_1 < \sigma_2$). Two parameters are determined by equating the variance $\sigma^2 = a\sigma_1^2 + (1-a)\sigma_2^2$ and excess kurtosis $k = \kappa - 3 = 3a(1-a)(\sigma_1^2 - \sigma_2^2)^2 / \sigma^4$ of $g(A)$ to that of the data. We then perform a least-squares fit of the cumulative density function of the data to solve for the remaining degree of freedom a . (See Appendix B for details.)

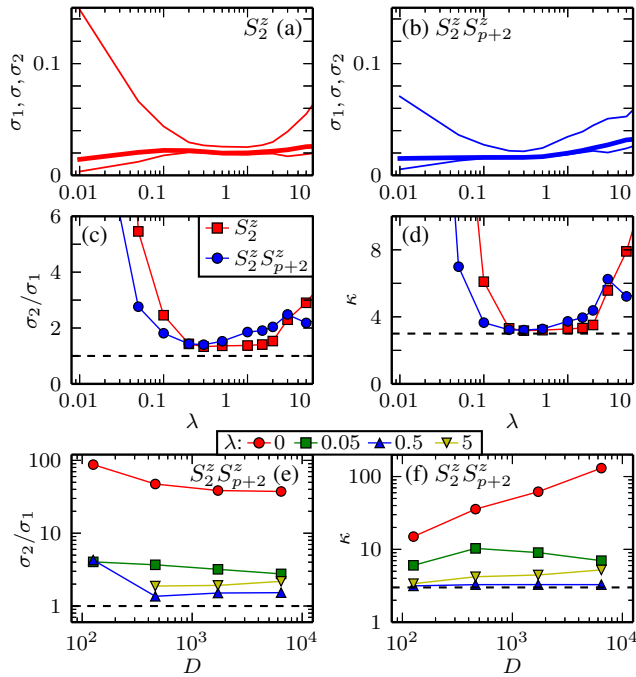


FIG. 4. Characteristics of the distribution of $A_{\alpha\beta}$. (a,b) Standard deviations σ_1, σ , and σ_2 of the “inner” gaussian of Eq. (8), the full distribution, and the “outer” gaussian, in increasing order. The thicker curve is σ . System size is $(L, N_\uparrow) = (15, 7)$. (c,d) Ratio σ_1/σ_2 and kurtosis κ . The dashed horizontal lines are the values for the gaussian distribution ($\sigma_2/\sigma_1 = 1$, $\kappa = 3$). We show results for $\hat{A} = S_2^z$ in red (squares) and for $\hat{A} = S_2^z S_{p+2}^z$ in blue (circles). (e,f) σ_2/σ_1 and κ as a function of the Hilbert-space dimension D for several values of λ . In (e), data for the smallest system size for $\lambda = 5$ is absent — the procedure does not yield a solution for σ_i due to the low density of states.

The resulting distributions $g(A)$ are plotted in Fig. 3 as dashed curves. The two-gaussian form works very well for small λ , and reasonably well for large λ . The discrepancy in Fig. 3(f) may be simply due to the lack of sufficient data points to provide good statistics for these particular parameters.

In Fig. 4, we show data related to this two-component description ($\sigma_{1,2}$, σ , κ), for the observables S_2^z and $S_2^z S_{p+2}^z$ in the ladder system. The two standard deviations generally become equal at intermediate λ (the ratio σ_2/σ_1 drops to near unity), indicating that a single-gaussian description works well away from integrability. In (d), we show the kurtosis κ of the distribution, used as an input for the fit. The kurtosis is close to 3 (the kurtosis value of the gaussian distribution) in the intermediate regime, again showing that a single gaussian is a good description for the distribution of $A_{\alpha\beta}$ values in generic systems. The kurtosis is significantly larger than 3 as one approaches the integrable points, signifying a stronger central peak than that of a single gaussian.

In Figs. 4(e) and (f), we provide a scaling analysis by plotting σ_2/σ_1 and κ as a function of the Hilbert-space dimension D for the observable $\hat{A} = S_2^z S_{p+2}^z$. In the non-integrable regime, the values remain near $\sigma_2/\sigma_1 \approx 1$ and $\kappa \approx 3$ as

the sizes are increased. For $\lambda = 0$, the kurtosis κ increases away from 3 with larger D , indicating that the central peak gets stronger relative to the larger gaussian as the system size increases. This is consistent with our explanation of the two-component structure in terms of symmetry sectors: the number of eigenstate pairs belonging to different sectors increases faster with D compared to the number of eigenstate pairs within the same symmetry sector.

Also noteworthy is the behavior at the near-integrable point $\lambda = 0.05$: the data shows convergence with increasing D toward the non-integrable values $\sigma_2/\sigma_1 = 1$ and $\kappa = 3$. In particular κ shows non-monotonic behavior: it first increases like in the integrable case, and only beyond a certain size starts decreasing back toward the single-gaussian value $\kappa = 3$. This is a manifestation of the phenomenon that, near but not exactly at integrability, the system size needs to be large to show generic non-integrable behavior [7].

V. SCALING ANALYSIS

In this section we analyze the system-size dependence of the average magnitudes of $|A_{\alpha\beta}|^2$, which corresponds to the widths of the distributions studied in the previous section.

The average value of $|A_{\alpha\beta}|^2$ close to the diagonal in the central part of the spectrum (omitting the lowest and highest 25% of the energy range, as indicated by the dashed squares in Fig. 1) is given by

$$\bar{\gamma} = \frac{1}{\tilde{N}} \sum_{\substack{\alpha, \beta \\ \alpha \neq \beta \\ |E_\beta - E_\alpha| \leq \omega_{\max}}} |A_{\alpha\beta}|^2 = S_A^2(0, \omega_{\max}). \quad (9)$$

Here, $\tilde{\Sigma}$ denotes summation over the relevant state pairs: It includes all α and β within the bulk of the spectrum with $\alpha \neq \beta$ and with $|E_\alpha - E_\beta| \leq \omega_{\max}$, where ω_{\max} acts as the frequency cutoff.

The quantity $\bar{\gamma}$ depends on the cutoff frequency ω_{\max} . We consider two values of ω_{\max} . First, we define a low-frequency measure, $\bar{\gamma}_{\text{low}} = \bar{\gamma}(\omega_{\max} = 0.05\omega_0)$, where ω_0 is the “typical frequency” [Eq. (6)]. Second, we define $\bar{\gamma}_{\text{all}} = \bar{\gamma}(\omega_{\max} \rightarrow \infty)$ including all state pairs within the bulk of the spectrum (dashed square in Figure 1).

In Fig. 5, we plot the quantities $\bar{\gamma}_{\text{low}}$, $\bar{\gamma}_{\text{all}}$, and the ratio $\bar{\gamma}_{\text{low}}/\bar{\gamma}_{\text{all}}$ as a function of Hilbert-space size D for several values of λ , in the top row for the observable $\hat{A} = S_2^z$ and in the lower row for $\hat{A} = S_2^z S_{p+2}^z$. Both $\bar{\gamma}_{\text{low}}$ and $\bar{\gamma}_{\text{all}}$ show a power-law behavior, $\propto D^{-1}$. The scaling is almost exact for $\bar{\gamma}_{\text{all}}$. This scaling behavior is consistent with the scaling of the temporal fluctuations being exponential in L , as observed in Ref. [14].

The D^{-1} scaling for non-integrable systems argued using the central limit theorem invoked in the previous section to explain the gaussian form of the distribution of $A_{\alpha\beta}$ values. From Eq. (7), we interpret $A_{\alpha\beta}$ as the average of the random variables $X_\gamma \equiv D c_\gamma^{(\alpha)*} c_\gamma^{(\beta)} a_\gamma$. Assuming $c_\gamma^{(\alpha)}$ and

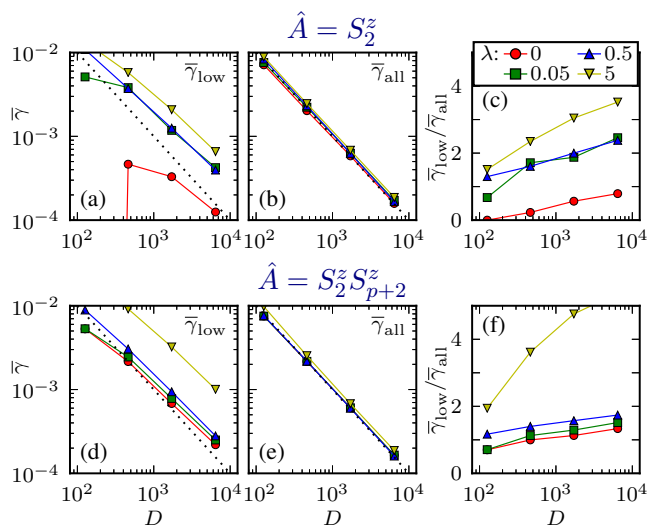


FIG. 5. System-size scaling analysis of average $|A_{\alpha\beta}|^2$ through the quantities (a) $\bar{\gamma}_{\text{low}}$, (b) $\bar{\gamma}_{\text{all}}$, and (c) $\bar{\gamma}_{\text{low}}/\bar{\gamma}_{\text{all}}$ for the observable $\hat{A} = S_2^z$, for several values of λ . The respective results for $\hat{A} = S_2^z S_{p+2}^z$ are shown in panels (d–f). The dotted lines in (a), (b), (d) and (e) are $\bar{\gamma} = 1/D$.

$c_\gamma^{(\beta)}$ to be independent random variables, each with variance $\sim 1/D$ due to normalization of the eigenfunctions, the random variable X_γ can be argued to have D -independent variance, $\text{var}(X_\gamma) \sim 1$. The central limit theorem then states that the variance of $A_{\alpha\beta}$ (i.e., the average of $|A_{\alpha\beta}|^2$) scales as $\text{var}(X_\gamma)/D \sim 1/D$. As in Ref. [7], the argument relies on difficult-to-prove randomness assumptions.

The D^{-1} scaling can be more directly understood by estimating the average value of all $|A_{\alpha\beta}|^2$, including the edges of the spectrum and the diagonal elements, which is equal to $\text{Tr}(A^2)/D^2$. For local observables, $\text{Tr}(A^2) \propto D$. (In fact, for the two observables in Fig. 5, $\text{Tr}(A^2) = D$ exactly.) The scaling of the average as $\propto D^{-1}$ immediately follows. Of course, both $\bar{\gamma}_{\text{all}}$ and $\bar{\gamma}_{\text{low}}$ are slightly different from $\text{Tr}(A^2)/D^2$. For $\bar{\gamma}_{\text{all}}$, the states outside the central part and the diagonal elements are not included, as opposed to $\text{Tr}(A^2)/D^2$ where they are included. Nevertheless, in Fig. 5(b,e), $\bar{\gamma}_{\text{all}}$ (data points) follows $\text{Tr}(A^2)/D^2 = 1/D$ (dotted line) very closely, for all λ . This shows that the contribution from the diagonal elements and from the edge states are negligible.

In Fig. 5(a,d), $\bar{\gamma}_{\text{low}}$ shows approximate $\propto D^{-1}$ scaling. The magnitudes are generally larger than $1/D$ for larger D , reflecting the fact that the low-frequency $|A_{\alpha\beta}|$ are on average larger than other off-diagonal matrix elements (as seen previously in Figs. 1 and 2). This is also reflected, Fig. 5(c,f), in the ratio $\bar{\gamma}_{\text{low}}/\bar{\gamma}_{\text{all}}$. The ratio > 1 for larger sizes. The effect is most prominent for large λ , which reflects the very large concentration near the diagonal seen in Figs. 1(c) and 2(c). The ratios $\bar{\gamma}_{\text{low}}/\bar{\gamma}_{\text{all}}$ increase with system size. It is conceivable that these ratios will converge to a constant at larger D , so that $\bar{\gamma}_{\text{low}}$ also converges to a $\propto D^{-1}$ dependence. The available data hints at such behavior, but the available systems sizes are insufficient to make a definitive statement.

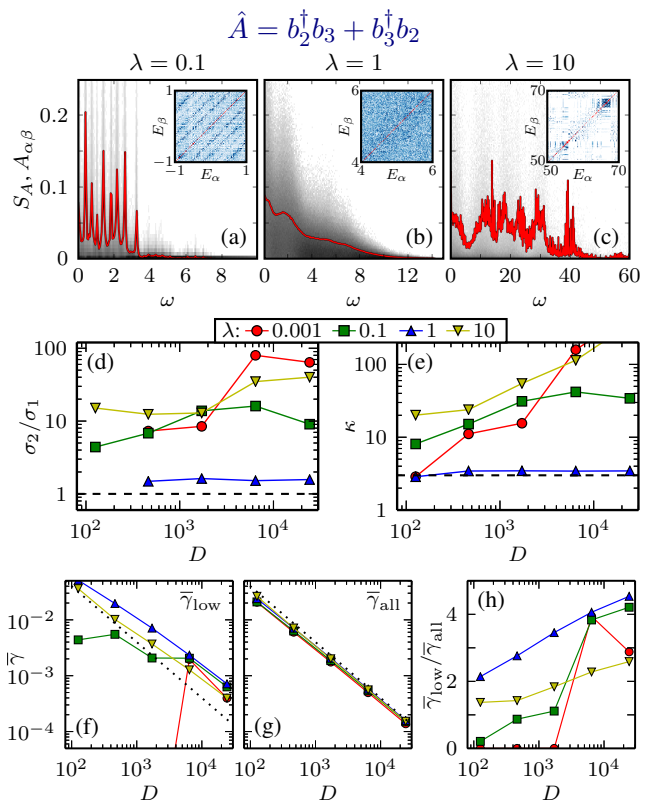


FIG. 6. Bose-Hubbard model; observable $\hat{A} = b_2^\dagger b_3 + b_3^\dagger b_2$. (a,b,c) Frequency-dependence shown through S_A , as in Fig. 2. Insets show fragments of the density plot of $|A_{\alpha\beta}|$ as function of E_α and E_β , as in Fig. 1. The system size is $(L, N_b) = (7, 7)$. (d,e) Analysis of the shape of the distribution through σ_2/σ_1 and kurtosis κ , as in Fig. 4. (f,g,h) Average matrix element $\bar{\gamma}_{\text{low}}$ and $\bar{\gamma}_{\text{all}}$ for low and all frequencies, and their ratio, as in Fig. 5. In (f,g), the dotted lines are $\bar{\gamma} = 4/D$.

The scaling of $\bar{\gamma}_{\text{low}}$ deviates from the $\propto D^{-1}$ especially for smaller systems and close to integrability. This behavior is reminiscent of the fluctuations of $A_{\alpha\alpha}$ close to (but not exactly at) an integrable point, where the scaling deviates from $D^{-1/2}$ for intermediate sizes but converges to $D^{-1/2}$ as the system size is increased [7].

VI. BOSE-HUBBARD CHAIN

To evaluate the generality of the results presented in previous sections with the XXZ ladder system, we present in this section a summary of analogous data for the Bose-Hubbard chain, Eq. (3). We show data for the observable $\hat{A} = b_2^\dagger b_3 + b_3^\dagger b_2$.

The frequency-resolved analysis of the matrix elements $A_{\alpha\beta}$ is performed for the values $\lambda = 1$, typical for the nonintegrable regime, and $\lambda = 0.1$ and 10 close to the two integrable limits. The results, in Figs. 6(a)–(c), are qualitatively similar to the ones for the XXZ model in Fig. 2.

In Figs. 6(d) and (e), we analyze the distribution of the val-

ues $A_{\alpha\beta}$ for low frequencies, by fitting to the two-component distribution as described in Sect. IV. The ratio σ_2/σ_1 and the kurtosis κ are high ($\gg 1$ and $\gg 3$, respectively) at or near integrability. In the nonintegrable regime (represented by $\lambda = 1$), both quantities are close to the values appropriate for a gaussian distribution (1 and 3, respectively).

In Figs. 6(d)–(h) we show data for $\lambda = 10^{-3}$ as a substitute for the exact integrable point $\lambda = 0$, because the strong oscillations at $\lambda = 0$ make our procedure for extracting $\sigma_{1,2}$ (Appendix B) unreliable. At accessible sizes, the $\lambda = 10^{-3}$ data indeed shows size-dependence characteristic of integrable points: increase of $\kappa > 3$ with increasing system size. At some very large system size, $\kappa(D)$ is expected to decrease again. Such nonmonotonic behavior is a signature of proximity to integrability. The non-monotonic behavior is visible at available system sizes for the $\lambda = 0.1$ data.

The root-mean-squared $\bar{\gamma}_{\text{all}}$ [Fig. 6(g)] of the matrix elements $|A_{\alpha\beta}|^2$ without frequency cutoff shows a D^{-1} scaling, the values being close to $\text{Tr}(A^2)/D^2 = 4/D$ [67]. The scaling of $\bar{\gamma}_{\text{low}}$ is not equally clear at these sizes. The erratic behavior close to integrability is possibly due to the presence of many very sharp peaks in S_A , especially at low frequencies [see Fig. 6(a)].

VII. DISCUSSION

Motivated by the importance of off-diagonal matrix elements ($A_{\alpha\beta}$) of local operators in the physics of time evolution after a quantum quench, we have provided a detailed study of the statistical properties of such matrix elements, for systems with short-range interactions. Data on off-diagonal matrix elements have appeared in the non-equilibrium literature (e.g. [3, 6, 19]); the present work extends such work to provide a systematic account of these objects. We have chosen multiple observables and families of Hamiltonians, and have thus been able to extract general features. We have also elucidated the role of proximity to integrability as well as the approach to the thermodynamic limit.

The distribution of values of $A_{\alpha\beta}$ is gaussian for generic systems, but deviates in a particular way (stronger peak at zero, or mixture of two gaussian-like distributions) as one approaches integrability. We have used this to formulate a quantitative characterization of proximity to integrability, through the kurtosis κ of the distribution. We find $\kappa \sim 3$ for non-integrable (generic or chaotic) systems, and a larger κ that *increases with system size* for integrable systems. This distinction makes it possible to graphically represent our idea, formulated in Ref. [7], that distance from integrability can be characterized by a length scale—for near-integrable systems, the size-dependence $\kappa(D)$ shows an initial increase followed by a decrease beyond a certain size. This size D where $\kappa(D)$ is maximal characterizes the proximity to integrability, and increases as one approaches integrability.

The average magnitude of the matrix elements, $S^2(\omega)$ or $\bar{\gamma}$, determines the magnitude of temporal fluctuations of $\langle A \rangle(t)$ after a quantum quench. The scaling of this quantity for non-integrable systems, $\sim 1/D$, is consistent with the scaling of

temporal fluctuations known from the literature [14]. We also find that the low-frequency average is higher than the average over all frequencies, $\bar{\gamma}_{\text{low}} > \bar{\gamma}_{\text{all}}$ (Figs. 5,6), reflecting the overall decrease of $S(\omega)$ with increasing frequency (Fig. 2). This suggests that, for quenches in nonintegrable systems, low-frequency contributions are likely to dominate in the time evolution, regardless of whether or not the initial conditions are very local in energy.

The $\sim 1/D$ scaling can be argued from the central limit theorem assuming wavefunction coefficients of non-integrable Hamiltonians to be effectively random. This is a recurring assumption in this field (e.g., [7, 14, 42]), usually without rigorous proof. We have provided an alternate argument based on the trace of local operators, which turns out to work well for $\bar{\gamma}_{\text{all}}$.

The present work raises a number of questions for further study. As a new characterization of integrability, the double-peak structure of the $A_{\alpha\beta}$ distribution deserves to be better understood. The relative weight of the inner peak is presumably connected to the distribution of sizes of the many sectors that the Hilbert space is divided into, due to the many conservation laws present at integrability. A related question is the type of deviation from the gaussian shape of the $A_{\alpha\beta}$ distribution for systems with a few (nonzero but $O(L^0)$) conservation laws. It would also be interesting to find out whether the two-component versus gaussian (single-component) structures can be related to differences in real-time relaxation and fluctuation behaviors between integrable and non-integrable systems. Also, it is possible that our findings for near-integrable points might have consequences for “pre-thermalization” behaviors [39, 66].

ACKNOWLEDGMENTS

We thank P. Ribeiro and L. Santos for interesting discussions.

Appendix A: Time evolution and off-diagonal matrix elements

In this Appendix we outline some of the connections to time evolution which motivates the study of off-diagonal matrix elements.

We consider a isolated quantum system with Hamiltonian H , with eigenvalues E_α and eigenstates $|\psi_\alpha\rangle$. Under this Hamiltonian, the time evolution of the initial state $|\Psi(0)\rangle$, that may be the result of a quench at $t = 0$ from another Hamiltonian, is given by $|\Psi(t)\rangle = \sum_\alpha c_\alpha e^{-iE_\alpha t} |\psi_\alpha\rangle$, where $c_\alpha = \langle \psi_\alpha | \Psi(0) \rangle$ are the expansion coefficients in the eigenstate basis. Given an observable A , its expectation value evolves as

$$\langle A \rangle(t) = \langle \Psi(t) | \hat{A} | \Psi(t) \rangle = \sum_{\alpha,\beta} c_\alpha^* c_\beta A_{\alpha\beta} e^{i(E_\alpha - E_\beta)t}. \quad (\text{A1})$$

The long-time average of this quantity is

$$\overline{\langle A \rangle(t)} = \lim_{T \rightarrow \infty} \frac{1}{T} \int_0^T \langle A \rangle(t) dt. \quad (\text{A2})$$

For a non-degenerate spectrum, the off-diagonal terms do not contribute, so that $\langle A \rangle(t) = \sum_{\alpha} |c_{\alpha}|^2 A_{\alpha\alpha}$.

While the $A_{\alpha\alpha}$ determine the long-time average, these diagonal matrix elements do not say anything about the temporal fluctuations $f_A(t) \equiv \langle A \rangle(t) - \langle A \rangle$ around the average. A representative value for the magnitude of temporal fluctuations is its root-mean-square

$$(\sigma_A^t)^2 \equiv \overline{[f_A(t)]^2} = \lim_{T \rightarrow \infty} \frac{1}{T} \int_0^T [f_A(t)]^2 dt. \quad (\text{A3})$$

Using Eq. (A1), under the assumption that the spectrum is incommensurate, one finds

$$(\sigma_A^t)^2 = \sum_{\substack{\alpha, \beta \\ \alpha \neq \beta}} |c_{\alpha}|^2 |c_{\beta}|^2 |A_{\alpha\beta}|^2, \quad (\text{A4})$$

The fluctuation amplitude $(\sigma_A^t)^2$ can be considered as a correlator of $f_A(t)$ with itself. Generalizing to correlators at different times, we get the autocorrelation function,

$$\overline{f_A(t) f_A(t + \tau)} = \sum_{\substack{\alpha, \beta \\ \alpha \neq \beta}} |c_{\alpha}|^2 |c_{\beta}|^2 |A_{\alpha\beta}|^2 e^{i(E_{\beta} - E_{\alpha})\tau}, \quad (\text{A5})$$

which appears in formulations of non-equilibrium fluctuation-dissipation relations [19, 22]. The Fourier transform of this quantity is

$$s^2(\omega) = \sum_{\substack{\alpha, \beta \\ \alpha \neq \beta}} |c_{\alpha}|^2 |c_{\beta}|^2 |A_{\alpha\beta}|^2 \delta(\omega - (E_{\beta} - E_{\alpha})). \quad (\text{A6})$$

The strength of the fluctuations at frequency $E_{\beta} - E_{\alpha}$ is equal to $|c_{\alpha}|^2 |c_{\beta}|^2 |A_{\alpha\beta}|^2$.

Eqs. (A4) and (A6) demonstrate the roles of $A_{\alpha\beta}$ in real-time considerations. The quantity $\bar{\gamma}$ in our work can be regarded as a general version of the right hand side of (A4)

which is independent of any particular quench protocol. The quantity $S^2(\omega)$ is similarly a smoothed version of the right hand side of (A6), again omitting reference to specific initial states.

Appendix B: Fit to the distribution of $A_{\alpha\beta}$

In Sec. IV, we have fitted the sum of two gaussian distributions $g(A)$ [Eq. (8)] to the actual distribution $d(A)$ of the off-diagonal elements in a small frequency window. The fit parameters in this distribution are a , the mutual weight of the two terms, and σ_1 and σ_2 , the standard deviations. For the fits shown in Fig. 3 and for the data plotted in Fig. 4, we impose that the fitted distribution $g(A)$ has the same variance σ^2 and kurtosis κ as the actual data. This yields the equations $\sigma^2 = a\sigma_1^2 + (1-a)\sigma_2^2$ and $\kappa - 3 = 3a(1-a)(\sigma_1^2 - \sigma_2^2)^2/\sigma^4$. By solving these equations for given σ^2 and $k = \kappa - 3$, we obtain expressions for σ_1 and σ_2 in terms of a ,

$$\begin{aligned} \sigma_1^2 &= \sigma^2 \left(1 - \sqrt{\frac{1}{3}k(1-a)/a} \right), \\ \sigma_2^2 &= \sigma^2 \left(1 + \sqrt{\frac{1}{3}ka/(1-a)} \right), \end{aligned} \quad (\text{B1})$$

where we have imposed the constraint $\sigma_1^2 \leq \sigma^2 \leq \sigma_2^2$. The remaining variable a can be obtained in several ways. For Figs. 3 and 4, we have obtained a by numerically minimizing the integrated square difference between the cumulative density function of $g(A)$ and that of the data $d(A)$. This method yields an ‘‘optimal’’ value of a , which is substituted into Eq. (B1) in order to obtain σ_1 and σ_2 . However, when the cumulative density distribution of the data behaves erratically due to very few states being involved, this procedure might fail and give an optimal value of a outside the range $[0, 1]$ (e.g., the $\lambda = 5$ data in Fig. 4).

-
- [1] J. M. Deutsch, Phys. Rev. A **43**, 2046 (1991).
 - [2] M. Srednicki, Phys. Rev. E **50**, 888 (1994).
 - [3] M. Rigol, V. Dunjko, and M. Olshanii, Nature **452**, 854 (2008).
 - [4] T. N. Ikeda, Y. Watanabe, and M. Ueda, Phys. Rev. E **87**, 012125 (2013).
 - [5] M. Rigol and M. Srednicki, Phys. Rev. Lett. **108**, 110601 (2012).
 - [6] R. Steinigeweg, J. Herbrych, and P. Prelovšek, Phys. Rev. E **87**, 012118 (2013).
 - [7] W. Beugeling, R. Moessner, and M. Haque, Phys. Rev. E **89**, 042112 (2014).
 - [8] M. Rigol, Phys. Rev. Lett. **103**, 100403 (2009).
 - [9] M. Rigol, Phys. Rev. A **80**, 053607 (2009).
 - [10] E. Khatami, M. Rigol, A. Relaño, and A. M. García-García, Phys. Rev. E **85**, 050102 (2012).
 - [11] C. Gramsch and M. Rigol, Phys. Rev. A **86**, 053615 (2012).
 - [12] K. He, L. F. Santos, T. M. Wright, and M. Rigol, Phys. Rev. A **87**, 063637 (2013).
 - [13] S. Ziraldo and G. E. Santoro, Phys. Rev. B **87**, 064201 (2013).
 - [14] P. R. Zangara, A. D. Dente, E. J. Torres-Herrera, H. M. Pastawski, A. Iucci, and L. F. Santos, Phys. Rev. E **88**, 032913 (2013).
 - [15] P. Reimann, Phys. Rev. Lett. **101**, 190403 (2008).
 - [16] A. J. Short, New J. Phys. **13**, 053009 (2011).
 - [17] N. Linden, S. Popescu, A. J. Short, and A. Winter, Phys. Rev. E **79**, 061103 (2009).
 - [18] L. C. Venuti and P. Zanardi, Phys. Rev. E **87**, 012106 (2013).
 - [19] E. Khatami, G. Pupillo, M. Srednicki, and M. Rigol, Phys. Rev. Lett. **111**, 050403 (2013).
 - [20] M. Fagotti, M. Collura, F. H. L. Essler, and P. Calabrese, Phys. Rev. B **89**, 125101 (2014).
 - [21] M. Fagotti and F. H. L. Essler, Phys. Rev. B **87**, 245107 (2013).
 - [22] M. Srednicki, J. Phys. A **32**, 1163 (1999).
 - [23] S. Ziraldo, A. Silva, and G. E. Santoro, Phys. Rev. Lett. **109**, 247205 (2012).

- [24] L. F. Santos, F. Borgonovi, and F. M. Izrailev, Phys. Rev. E **85**, 036209 (2012).
- [25] E. J. Torres-Herrera and L. F. Santos, Phys. Rev. E **88**, 042121 (2013).
- [26] L. F. Santos and M. Rigol, Phys. Rev. E **82**, 031130 (2010).
- [27] G. P. Brandino, A. De Luca, R. M. Konik, and G. Mussardo, Phys. Rev. B **85**, 214435 (2012).
- [28] E. Canovi, D. Rossini, R. Fazio, G. E. Santoro, and A. Silva, Phys. Rev. B **83**, 094431 (2011).
- [29] A. C. Cassidy, C. W. Clark, and M. Rigol, Phys. Rev. Lett. **106**, 140405 (2011).
- [30] J.-S. Caux and F. H. L. Essler, Phys. Rev. Lett. **110**, 257203 (2013).
- [31] S. Dubey, L. Silvestri, J. Finn, S. Vinjanampathy, and K. Jacobs, Phys. Rev. E **85**, 011141 (2012).
- [32] M. Fagotti and F. H. L. Essler, J. Stat. Mech. **2013**, P07012 (2013).
- [33] M. Fagotti, Phys. Rev. B **87**, 165106 (2013).
- [34] J. Gemmer, M. Michel, and G. Mahler, *Quantum Thermodynamics* (Springer Berlin Heidelberg, 2009).
- [35] S. Genway, A. F. Ho, and D. K. K. Lee, Phys. Rev. A **86**, 023609 (2012).
- [36] S. Goldstein, J. L. Lebowitz, R. Tumulka, and N. Zanghi, Phys. Rev. Lett. **96**, 050403 (2006).
- [37] K. He and M. Rigol, Phys. Rev. A **85**, 063609 (2012).
- [38] M. Eckstein and M. Kollar, Phys. Rev. Lett. **100**, 120404 (2008).
- [39] M. Kollar, F. A. Wolf, and M. Eckstein, Phys. Rev. B **84**, 054304 (2011).
- [40] V. K. B. Kota, A. Relaño, J. Retamosa, and M. Vyas, J. Stat. Mech. **2011**, P10028 (2011).
- [41] A. Motohashi, Phys. Rev. A **84**, 063631 (2011).
- [42] C. Neuenhahn and F. Marquardt, Phys. Rev. E **85**, 060101 (2012).
- [43] M. Rigol, V. Dunjko, V. Yurovsky, and M. Olshanii, Phys. Rev. Lett. **98**, 050405 (2007).
- [44] M. Rigol and L. F. Santos, Phys. Rev. A **82**, 011604 (2010).
- [45] G. Roux, Phys. Rev. A **81**, 053604 (2010).
- [46] G. Roux, Phys. Rev. A **79**, 021608 (2009).
- [47] J. Sirker, N. P. Konstantinidis, F. Andraschko, and N. Sedlmayr, Phys. Rev. A **89**, 042104 (2014).
- [48] S. Genway, A. F. Ho, and D. K. K. Lee, Phys. Rev. Lett. **111**, 130408 (2013).
- [49] H. Niemeyer, K. Michielsen, H. De Raedt, and J. Gemmer, Phys. Rev. E **89**, 012131 (2014).
- [50] R. Steinigeweg, A. Khodja, H. Niemeyer, C. Gogolin, and J. Gemmer, Phys. Rev. Lett. **112**, 130403 (2014).
- [51] E. J. Torres-Herrera and L. F. Santos, Phys. Rev. A **89**, 043620 (2014).
- [52] M. C. Bañuls, J. I. Cirac, and M. B. Hastings, Phys. Rev. Lett. **106**, 050405 (2011).
- [53] M. Marcuzzi, J. Marino, A. Gambassi, and A. Silva, Phys. Rev. Lett. **111**, 197203 (2013).
- [54] M. Collura, S. Sotiriadis, and P. Calabrese, Phys. Rev. Lett. **110**, 245301 (2013).
- [55] M. Collura, M. Kormos, and P. Calabrese, J. Stat. Mech. **2014**, P01009 (2014).
- [56] L. Masanes, A. J. Roncaglia, and A. Acín, Phys. Rev. E **87**, 032137 (2013).
- [57] G. Biroli, C. Kollath, and A. M. Läuchli, Phys. Rev. Lett. **105**, 250401 (2010).
- [58] A. Polkovnikov, K. Sengupta, A. Silva, and M. Vengalattore, Rev. Mod. Phys. **83**, 863 (2011).
- [59] T. N. Ikeda, Y. Watanabe, and M. Ueda, Phys. Rev. E **84**, 021130 (2011).
- [60] T. Barthel and U. Schollwöck, Phys. Rev. Lett. **100**, 100601 (2008).
- [61] M. Cramer, C. M. Dawson, J. Eisert, and T. J. Osborne, Phys. Rev. Lett. **100**, 030602 (2008).
- [62] M. Cramer and J. Eisert, New J. Phys. **12**, 055020 (2010).
- [63] J. M. Zhang, C. Shen, and W. M. Liu, Phys. Rev. A **83**, 063622 (2011).
- [64] J. M. Zhang, C. Shen, and W. M. Liu, Phys. Rev. A **85**, 013637 (2012).
- [65] J. M. Zhang, F. C. Cui, and J. Hu, Phys. Rev. E **85**, 041138 (2012).
- [66] M. Moeckel and S. Kehrein, Phys. Rev. Lett. **100**, 175702 (2008).
- [67] Here, $\text{Tr}(A^2) = \binom{L+N_b}{L-1} = 2D(L+N_b)N_b/L(L+1)$ which equals $4DL/(L+1)$ if $N_b = L$, i.e., at unit filling.